Barchan-barchan repulsion investigated at the grain scale

N. C. Lima[1], W. R. Assis[1,3], C. A. Alvarez[2], E. M. Franklin[1]

[1]Faculdade de Engenharia Mecânica, Universidade Estadual de Campinas (UNICAMP), Rua Mendeleyev, 200, Campinas, SP, Brazil
[2]Department of Earth & Planetary Sciences, Stanford University, Stanford, CA 94305, USA
[3]Current address: Saint Anthony Falls Laboratory, University of Minnesota, Minneapolis, Minnesota, USA

Key Points:

- We investigate numerically both the fluid flow and motion of grains for understanding the mechanisms behind barchan-barchan repulsion
- We measure the flow rate of grains and show that there is, indeed, greater erosion on the downstream barchan
- The disturbed flow impacting the downstream barchan induces higher erosion (of its grains) and low accumulation (of upstream grains)

Corresponding author: Erick M. Franklin, `erick.franklin@unicamp.br`

Abstract

Barchans are dunes of crescent shape found on Earth, Mars and other celestial bodies. Among the different types of barchan-barchan interaction, there is one, known as chasing, in which the dunes remain close but without touching each other. In this paper, we investigate the origins of this barchan-barchan repulsion by carrying out grain-scale numerical computations in which a pair of granular heaps is deformed by the fluid flow into barchan dunes that interact with each other. In our simulations, data such as position, velocity and resultant force are computed for each individual particle at each time step, allowing us to measure details of both the fluid and grains that explain the repulsion. We show the trajectories of grains, time-average resultant forces, and mass balances for each dune, and that the downstream barchan shrinks faster than the upstream one, keeping, thus, a relatively high velocity although in the wake of the upstream barchan. In its turn, this fast shrinkage is caused by the flow disturbance, which induces higher erosion on the downstream barchan and its circumvention by grains leaving the upstream dune. Our results help explaining the mechanisms behind the distribution of barchans in dune fields found on Earth and Mars.

Plain Language Summary

Barchans are crescent-shaped dunes with horns pointing downstream, formed by the action of a roughly unidirectional flow over a limited quantity of sand. These bedforms are usually found in barchan fields on Earth and Mars, where barchans interact with each other. Among the different types of barchan-barchan interaction, there is one in which the dunes remain close but without touching each other, known as chasing. In this paper, we investigate the barchan-barchan chasing by carrying out numerical simulations in which we compute the fluid flow and the dynamics of each individual grain for a pair of barchans interacting with each other. We show the trajectories of grains, time-average resultant forces, and mass balances for each dune, and that the downstream barchan shrinks faster than the upstream one, keeping, thus, a relatively high velocity although in the wake of the upstream barchan. We also show that the faster shrinkage is caused by the flow disturbance, which induces higher erosion (of its grains) and low accumulation (of grains leaving the upstream dune) on the downstream barchan. Our results provide new insights into the distribution of barchans found on Earth, Mars, and other celestial bodies.

1 Introduction

Barchans are dunes of crescent shape formed by the action of a roughly unidirectional flow over a limited quantity of sand, being commonly found in dune fields on Earth, Mars and other celestial bodies (Bagnold, 1941; Herrmann & Sauermann, 2000; Hersen, 2004; Elbelrhiti et al., 2005; Claudin & Andreotti, 2006; E. J. R. Parteli & Herrmann, 2007; Courrech du Pont, 2015). Within those fields, corridors of size-selected barchans are frequently observed, where intricate barchan-barchan interactions have proven essential for size regulation (Hersen et al., 2004; Hersen & Douady, 2005; Kocurek et al., 2010; Génois, Hersen, et al., 2013; Génois, du Pont, et al., 2013; Assis & Franklin, 2020, 2021; Assis et al., 2022). Among the different types of barchan-barchan interaction, there is one, known as chasing (Assis & Franklin, 2020, 2021), in which the dunes remain close but without touching each other. This interaction pattern is, in a certain way, counter-intuitive, since the downstream dune is in the wake of that upstream. However, Assis and Franklin (2021) showed that the downstream dune erodes faster than the upstream one, decreasing in size and increasing is speed, outrunning then the upstream dune.

The short-range interaction of barchans, including barchan-barchan collision (i.e., when they touch each other), was the object of several studies over the last decades, most of them carrying out measurements of eolian barchans (Norris & Norris, 1961; Gay, 1999;

Vermeesch, 2011; Elbelrhiti et al., 2008; Hugenholtz & Barchyn, 2012), experiments with aquatic barchans (Endo et al., 2004; Hersen & Douady, 2005), and numerical simulations (A. Lima et al., 2002; E. Parteli & Herrmann, 2003; Schwämmle & Herrmann, 2003; Durán et al., 2005, 2009; Katsuki et al., 2011; Génois, du Pont, et al., 2013; X. Zhou et al., 2019). Although they increased considerably our knowledge on barchan-barchan interactions, those studies have some drawbacks. In the eolian case, time series for barchan-barchan interactions are incomplete, given their long timescale (of the order of decades). In the case of numerical simulations, they consisted of continuous, simplified discrete, or agent-based models, so that they contained simplifications that precluded some interaction patterns of taking place. In common, these studies measured or computed the dynamics of barchans at the bedform scale, and, therefore, the dynamics at the grain scale was not known.

To the authors' knowledge, the first study to inquire specifically into the dune-dune repulsion mechanism was Bacik et al. (2020), who investigated experimentally the dynamics of a pair of two-dimensional (2D) dunes in a narrow Couette-type circular channel. In their experiments, they placed two piles of grains inside the channel filled with water, and paddles on the water free surface imposed a turbulent flow that deformed the piles into two-dimensional dunes that interacted with each other over long times. For this 2D case, the authors found that turbulent structures formed in the wake of bedforms induce dune-dune repulsion, preventing dunes from touching each other. Bacik et al. (2020) inferred that the same mechanism could be also valid for two barchans of comparable size, which was later proved true by Assis and Franklin (2020, 2021). As previous studies, Bacik et al. (2020) conducted measurements at the bedform scale.

Recently, we inquired into barchan-barchan interactions by conducting experiments in a water tank (Assis & Franklin, 2020, 2021; Assis et al., 2022), with measurements carried out at both the bedform and grain scales. In the experiments, the initial configurations (aligned or off-centered), initial conditions, grain types (diameter, density and roundness), pile masses, initial distances, and water flow rates were varied, and from the results we found five interaction patterns for both aligned and off-centered configurations: (i) chasing, when dunes do not touch each other; (ii) merging, when collision occurs and the dunes merge; (iii) exchange, when collision occurs and, just afterward, a small barchan is ejected; (iv) fragmentation-chasing, when collision does not occur and the downstream dune splits; and (v) fragmentation-exchange, when fragmentation initiates before collision with one of the split parts takes place. Although our findings explained some aspects of interactions at the grain scale, information such as forces acting on each grain and the dynamics of hidden (totally or partially buried) grains were not accessible. In another front, following Alvarez and Franklin (2020, 2021), we carried out CFD-DEM (computational fluid dynamics - discrete element method) of isolated barchan dunes (N. C. Lima et al., 2022). In the simulations, we used LES (large eddy simulation) for the fluid, with the smaller scales of the order of the grain diameter. With those simulations, we could measure information missing in experiments, such as those listed above (forces on each grain, for instance). To the best of our knowledge, these are the only grain scale simulations of barchans carried out to this date. If successfully conducted for barchan-barchan interactions, all the missing details for understanding the different patterns would be available.

In this paper, we inquire into the origins of the repulsion mechanism of the chasing pattern by carrying out LES-DEM computations. In the simulations, solved at the scale of grains, a pair of granular heaps is deformed by a water flow into barchan dunes that interact with each other, and we compute data such as position, velocity and resultant force for each individual particle at each time step. We show the trajectories of grains, time-average resultant forces, and mass balances for each dune, and that the downstream barchan shrinks faster than the upstream one. Therefore, the downstream barchan keeps a relatively high velocity although in the wake of the upstream one. We also show that, in its turn, the fast shrinkage of the downstream barchan is caused by the flow disturbance, which induces higher erosion on the downstream barchan and its circumvention by grains leaving the upstream dune (so that deposition of grains from the upstream dune is small). Our results represent a contribution for understanding the mechanisms behind the distribution of barchans in dune fields on Earth, Mars, and other celestial bodies.

2 Materials and Methods

We carried out Euler-Lagrange simulations, in which the fluid flow is computed in an Eulerian grid while the solid particles are tracked in a Lagrangian framework. We used the same model described in N. C. Lima et al. (2022), where the fluid is solved with LES by using the open-source CFD code OpenFOAM (https://openfoam.org), and the motion of grains is solved with DEM by using the open-source code LIGGGHTS (Kloss & Goniva, 2010; Berger et al., 2015). The coupling between CFD and DEM is done by the open-source code CFDEM (www.cfdem.com, Goniva et al., 2012).

The Lagrangian part (DEM) computes the linear and angular momentum equations for each solid particle (grain), given by Equations 1 and 2, respectively,

$$m_p \frac{d\vec{u}_p}{dt} = \vec{F}_p \, , \tag{1}$$

$$I_p \frac{d\vec{\omega}_p}{dt} = \vec{T}_c \, , \tag{2}$$

where, for each grain, m_p is the mass, $\vec{u}_p$ is the velocity, I_p is the moment of inertia, $\vec{\omega}_p$ is the angular velocity, $\vec{T}_c$ is the resultant of contact torques between solids, and $\vec{F}_p$ is the resultant force (weight, contact and fluid forces), given by

$$\vec{F}_p = \vec{F}_{fp} + \vec{F}_c + m_p \vec{g} \, , \tag{3}$$

In Equation 3, $\vec{g}$ is the acceleration of gravity and, for each grain, $\vec{F}_c$ is the resultant of contact forces between solids and $\vec{F}_{fp}$ is the resultant of fluid forces. For the contact forces and torques, $\vec{F}_c$ and $\vec{T}_c$, respectively, we consider a Hertzian model, in which contact forces are decomposed into normal and tangential components, as shown briefly in the Supporting Information (for more details, see N. C. Lima et al., 2022). For the resultant of fluid forces, $\vec{F}_{fp}$, we consider Equation 4,

$$\vec{F}_{fp} = \vec{F}_d + \vec{F}_p + \vec{F}_\tau + \vec{F}_{vm} \, , \tag{4}$$

where $\vec{F}_d$ is the fluid drag, $\vec{F}_p$ is the force due to pressure gradient, $\vec{F}_\tau$ is the force due to the deviatoric stress tensor, and $\vec{F}_{vm}$ is the virtual mass force (we neglect the Basset, Saffman, and Magnus forces because they are usually negligible in CFD-DEM simulations, Z. Y. Zhou et al., 2010). As in previous works, we neglect torques caused directly by the fluid in the angular momentum (Equation 2), since those due to contacts are much higher (Tsuji et al., 1992, 1993; Liu et al., 2016).

Because the fluid is water, the Eulerian part (LES) computes the incompressible mass and momentum equations, given by Equations 5 and 6, respectively,

$$\nabla \cdot \vec{u}_f = 0 \, , \tag{5}$$

$$\frac{\partial \rho_f \vec{u}_f}{\partial t} + \nabla \cdot (\rho_f \vec{u}_f \vec{u}_f) = -\nabla P + \nabla \cdot \vec{\vec{\tau}} + \rho_f \vec{g} - \frac{N}{V} \vec{F}_{fp} \,, \tag{6}$$

where $\vec{u}_f$ is the fluid velocity, ρ_f is the fluid density, P the fluid pressure, $\vec{\vec{\tau}}$ the deviatoric stress tensor of the fluid, $\vec{g}$ is the acceleration of gravity, N is the number of grains in a given cell and V is the cell volume. More details of the used model and numerical implementation are available in N. C. Lima et al. (2022).

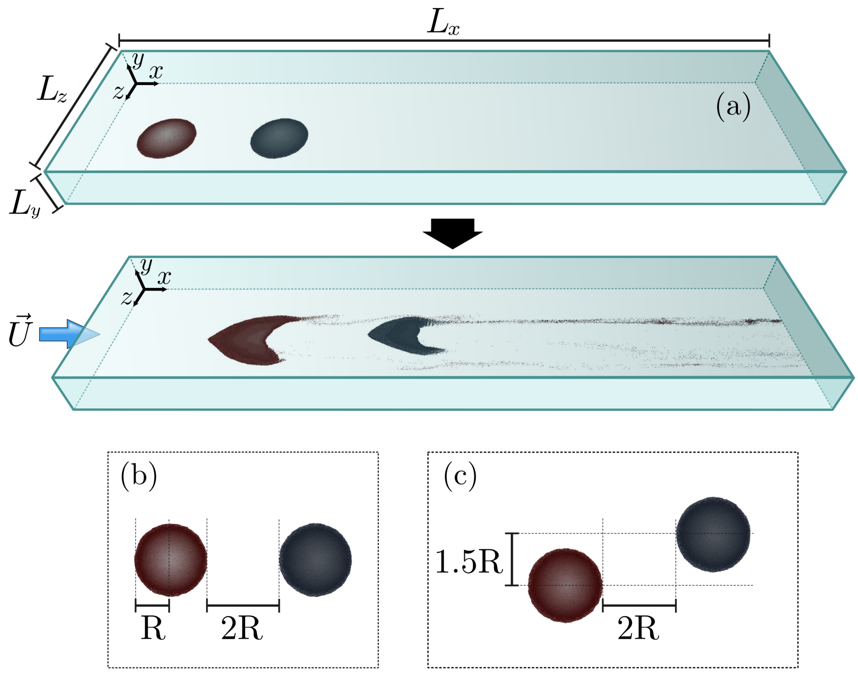

Figure 1. (a) Layout of the numerical setup, showing the channel dimensions, the flow direction, the initial piles, and their evolution at a posterior time. (b) and (c) Relative positions of the initial piles (top view) for the aligned and off-centered cases, respectively. In both cases, the upstream pile was initially placed at 3 cm from the CFD inlet.

The CFD domain consists in a 3D channel of size $L_x = 0.4$ m, $L_y = \delta = 0.025$ m and $L_z = 0.1$ m, where x, y and z are the longitudinal, vertical and spanwise directions, respectively. We note that, for saving computing time, the vertical dimension $L_y = \delta$ corresponds to the channel half height, i.e., the channel centerline (the real channel height is 2δ). With that, the CFD domain has periodic conditions in the longitudinal and spanwise directions, no-slip conditions on the bottom wall, and free slip on the top boundary ($y = \delta$). The channel Reynolds number based on the cross-sectional mean velocity U, Re $= U2\delta\nu^{-1}$, is 14,000, and the Reynolds number based on shear velocity u_*, Re$_*$ $= u_*\delta\nu^{-1}$, is 400, where ν is the kinematic viscosity of the water. The granular material forming each initial heap consisted of 10^5 glass spheres, with sizes randomly distributed (in a Gaussian distribution) within 0.15 mm $\leq d \leq$ 0.25 mm. The boundary conditions for the grains were solid wall at the bottom boundary, free exit at the outlet, and no grain influx at the inlet (the number of grains in the domain decreased along time, in the same way as in our previous experiments, Assis & Franklin, 2020, 2021; Assis et al., 2022). The current setup is similar to those shown in N. C. Lima et al. (2022), where the DEM and LES parameters were extensively tested and compared with experiments. Therefore, a complete description of CFD meshes and convergence, DEM parameters, and tests and validation can be found in N. C. Lima et al. (2022), and more details of the numerical setup are available in the Supporting Information.

Prior to simulations of barchan-barchan interactions, we carried out LES simulations of pure water flow in the periodic channel, until reaching a fully-developed turbulent flow. The results were stored to be used as initial condition for the fluid in the LES-DEM simulations. The next step was then to completely stop the water flow and let the grains settle by free fall, forming two conical piles with radius $R \approx 0.0145$ m and height $h \approx 0.003$ m. The piles were distant $2R$ from each other in the longitudinal direction, and either 0 (for the aligned case) or $1.5R$ (for the off-centered case) in transverse direction, as shown in Figures 1b and 1c, and the upstream pile was initially placed at 3 cm from the CFD inlet. The final step was, thus, to impose the turbulent flow stored in a previous step.

3 Results

3.1 Morphology

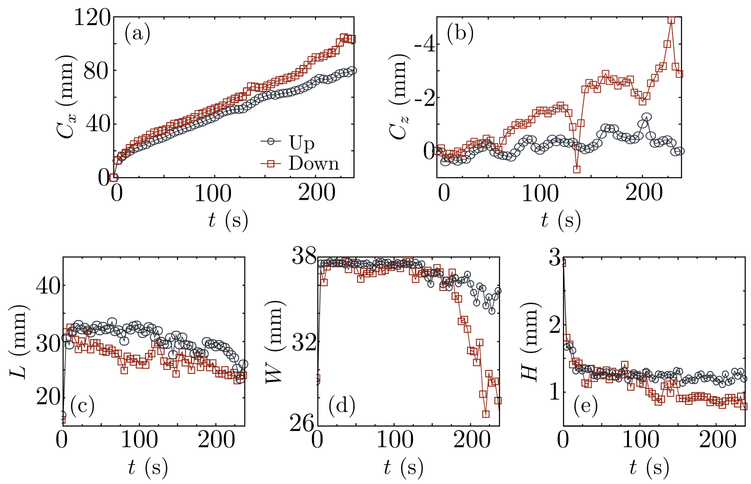

Figure 2. Morphodynamics of interacting barchans in the aligned case. (a) Longitudinal displacement C_x, (b) transverse displacement C_z, (c) length L, (d) width W, and (e) height H of barchans. In the graphics, *Up* stands for the upstream barchan and *Down* for the downstream barchan, and we fixed the origins of C_x and C_z of each dune in the centroid of the respective initial pile.

As soon as the water flow is imposed in the domain, the conical piles are deformed into two barchan dunes that interact with each other, as can be observed in the snapshots (with some transparency for better observing grain migration) of Figures 4a and 5a for the aligned and off-centered cases, respectively. Snapshots without transparency (Figure S1) and movies showing the evolution of bedforms are available in Supporting Information. The behavior for these flow conditions is similar to those observed in our previous experiments (Assis & Franklin, 2020, 2021), with the downstream barchan shrinking and moving faster than the upstream one (*chasing* pattern), most noticeable in the aligned case. This is evinced in Figures 2 and 3, showing the time evolution of longitudinal and transverse displacements (C_x and C_z, panels (a) and (b)), length (L, panel (c)), width (W, panel (d)), and height (H, panel (e)) of dunes for the aligned and off-centered cases, respectively. In Figures 2a-b and 3a-b, the longitudinal and transverse displacements were computed based on the centroid of each dune, and we fixed the origins of C_x

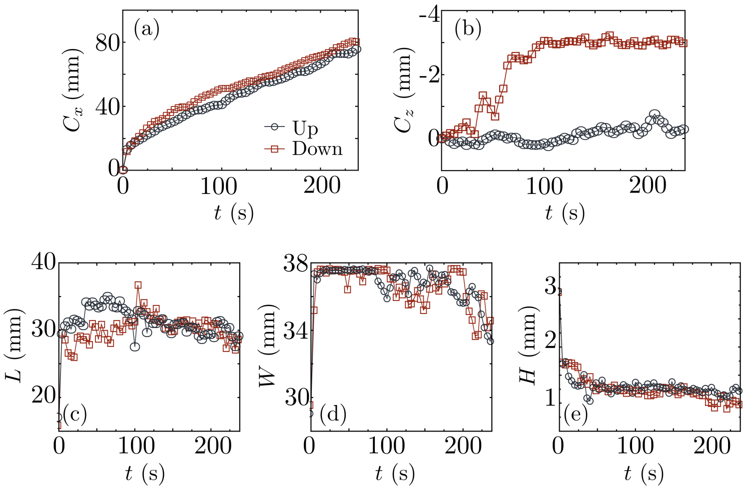

Figure 3. Morphodynamics of interacting barchans in the off-centered case. (a) Longitudinal displacement C_x, (b) transverse displacement C_z, (c) length L, (d) width W, and (e) height H of barchans. In the graphics, *Up* stands for the upstream barchan and *Down* for the downstream barchan, and we fixed the origins of C_x and C_z of each dune in the centroid of the respective initial pile.

and C_z in the centroid of the respective initial pile. In the aligned case, we observe a higher decrease in L, W and H for the downstream dune than for the upstream one, while its longitudinal displacement C_x increases faster than that of the upstream barchan, indicating an augmentation of the longitudinal separation along time. In the off-centered case, L, W, H and C_x vary in a similar way for both barchans, indicating that they keep roughly the same longitudinal separation along time. The variations in the longitudinal separation are visible in the snapshots shown in Figures 4a and 5a.

In both cases, the transverse displacement C_z of the upstream dune remains close to zero, while that of the downstream dune increases in modulus as a consequence of its motion in the transverse direction, as also observed in previous experiments (Assis & Franklin, 2020, 2021). The reason for the transverse motion is related to the exchange of grains between barchans, described in Subsection 3.2. In the aligned case, we note that Figure 2b shows two large peaks for C_z due to clumps of grains that are ejected from and/or absorbed by the downstream barchan.

3.2 Motion of grains and mass exchange

One advantage of discrete simulations in comparison with our previous experiments (Assis & Franklin, 2020, 2021) is the knowledge of the instantaneous position of all grains, and the possibility of tracking each one of them along time. With that, typical trajectories and velocities of grains can be computed, as well as the resultant force acting on each of them. Next, we will focus the discussion on grains exchanged between barchans, see Figure S2 in Supporting Information for graphics showing velocity fields of grains moving over barchans.

We, thus, inquired into the trajectories of grains that migrate from one barchan to the other, and identified the points of origin and destination of those grains in order to compute statistics and the mass flow rate by regions. For example, Figures 4b–d and 5b–d show a portion of the mass exchange between barchans for the aligned and off-centered cases, respectively. In Figures 4b and 5b, we plot trajectories of grains leaving the up-

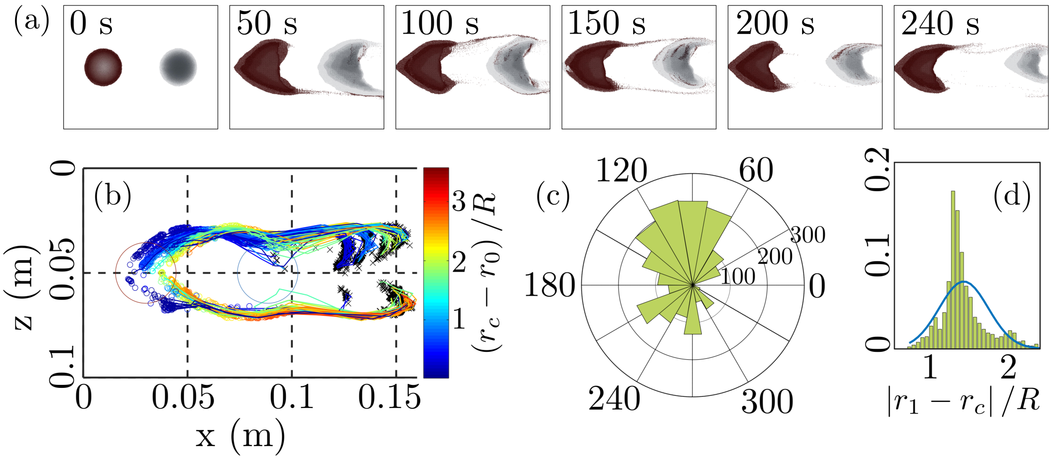

Figure 4. Mass exchange in the aligned case. (a) Snapshots with transparency showing the grains of each dune (top view) at different instants (appearing in maroon for the upstream barchan and gray for the downstream one due to the percentage of transparency adopted). (b) Trajectories of grains leaving the upstream barchan and reaching the downstream one, in which the colorbar indicates the dune longitudinal position when the considered grain started its motion. The large circles indicate the initial piles (top view), the small circles the initial position of the considered grain when it started moving on the upstream barchan, and the x's indicate their respective final positions (when stopping) on the downstream barchan. (c)–(d) Number of grains N from the upstream barchan reaching the downstream one, in polar coordinates (with origin on the centroid of the upstream barchan): (c) frequency of occurrence of N as a function of the angle (the origin is aligned with the flow direction), and (d) probability density function (pdf) of N as a function of the radial position. In the figure, R is the radius of the initial pile, r_1 is the initial radial position of grains leaving the upstream barchan, and r_c and r_0 are, respectively, the instantaneous and initial positions of the centroid of the upstream dune.

stream barchan and reaching the downstream one. In the figures, the colorbar indicates the dune longitudinal position when the considered grain started its motion, where r_c and r_0 are, respectively, the instantaneous and initial positions of the centroid of the upstream dune. Large circles represent the initial piles of radius R, small circles the initial position of the considered grain when it started moving on the upstream barchan, and the x's indicate their respective final positions (when stopping) on the downstream barchan. We note that we have not plotted in Figures 4b and 5b the lines corresponding to all trajectories (in order to avoid saturating the image with trajectory lines). All the circles and x's are, however, plotted in these figures, and we used a velocity threshold corresponding to $0.1u_*$ for the starting and ending of motions. We first observe (as well as in Figures 4a and 5a) that most of those grains, after leaving the upstream dune by its horns (or one of them in the off-centered case), circumvent the downstream dune until arriving in its lee-side/recirculation region, where they accumulate. The major difference between aligned and off-centered cases is that in the aligned case grains leaving both horns of the upstream barchan circumvent the downstream dune, while in the off-centered case only grains from one horn (the one closer to the downstream dune) circumvent the downstream barchan before settling on the lee side.

In order to analyze the ensemble of those migrating grains, we computed the number of grains N that left the upstream barchan and reached the downstream one (over

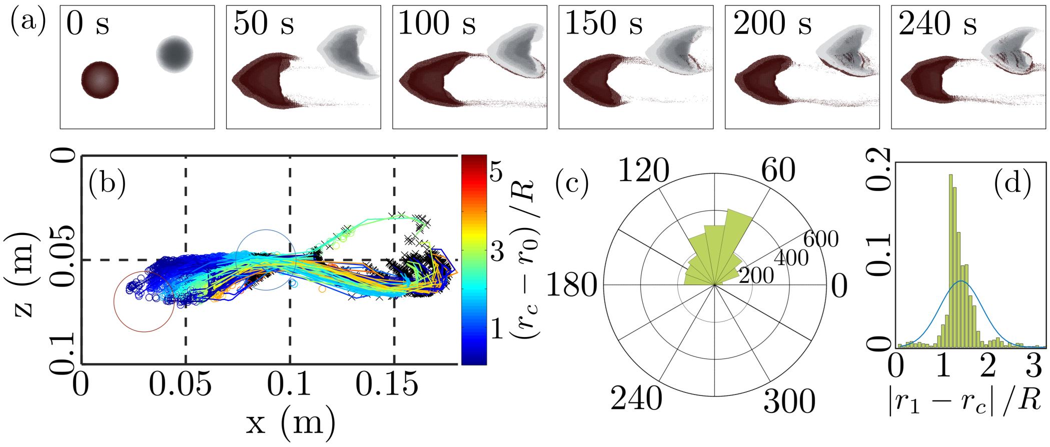

Figure 5. Mass exchange in the off-centered case. (a) Snapshots with transparency showing the grains of each dune (top view) at different instants (appearing in maroon for the upstream barchan and gray for the downstream one due to the percentage of transparency adopted). (b) Trajectories of grains leaving the upstream barchan and reaching the downstream one, in which the colorbar indicates the dune longitudinal position when the considered grain started its motion. The large circles indicate the initial piles (top view), the small circles the initial position of the considered grain when it started moving on the upstream barchan, and the x's indicate their respective final positions (when stopping) on the downstream barchan. (c)–(d) Number of grains N from the upstream barchan reaching the downstream one, in polar coordinates (with origin on the centroid of the upstream barchan): (c) frequency of occurrence of N as a function of the angle (the origin is aligned with the flow direction), and (d) pdf of N as a function of the radial position. In the figure, R is the radius of the initial pile, r_1 is the initial radial position of grains leaving the upstream barchan, and r_c and r_0 are, respectively, the instantaneous and initial positions of the centroid of the upstream dune.

240 s), and identified their respective positions of origin in polar coordinates (with coordinates' origin on the centroid of the upstream barchan). With these numbers, we computed the frequency of occurrence of N as a function of the angle, and the probability density function (pdf) of N as a function of the radial position, which are shown, respectively, in Figures 4c and 4d (for the aligned case) and 5c and 5d (for the off-centered case), where r_1 is the initial radial position of grains leaving the upstream barchan. We observe a large asymmetry in Figure 5c, which was already expected since the downstream barchan receives grains from just one of the horns of the upstream barchan, but there is also an asymmetry in the aligned case. In this latter case, due to initial fluctuations in the mass exchange, the downstream dune becomes asymmetrical and migrates in the transverse direction toward the horn that sheds more grains. This was observed in our previous experiments (Assis & Franklin, 2020, 2021), and can be also observed in Figure 4a. Therefore, in the off-centered case most grains migrating to the downstream barchan have their origin in the region close to one of the horns, while in the aligned case the migrating grains have their origin on the flanks of the upstream barchan, with an asymmetry that increases over time as the downstream dune moves in the transverse direction. As a consequence, in the aligned case those grains start moving in upstream regions near the dune flanks, follow a path along the periphery of the upstream barchan until reaching its horns, and from there are shed toward the downstream barchan, as can be seen in the movies S1 and S2 available in the Supporting Information and in those of Assis and Franklin (2021).

We note that in the aligned case part of the grains on the toe of the downstream barchan migrate toward the lee side of the upstream dune entrained by its recirculation region. Trajectories of grains migrating from the downstream to the upstream barchan are available in Figure S3 of Supporting Information. In addition, we computed the velocity field of moving grains, for which we present the time-averaged fields in Figure S2 of Supporting Information. We can observe larger velocities over the upstream barchan than over the downstream one, indicating that the larger erosion over the downstream dune is due to a larger density of moving grains. Indeed, this is the case for the aligned case at all times, and for the off-centered case at the beginning of interactions, as can be seen in the graphics of the density of moving grains shown in Figures S4 and S5 of Supporting Information.

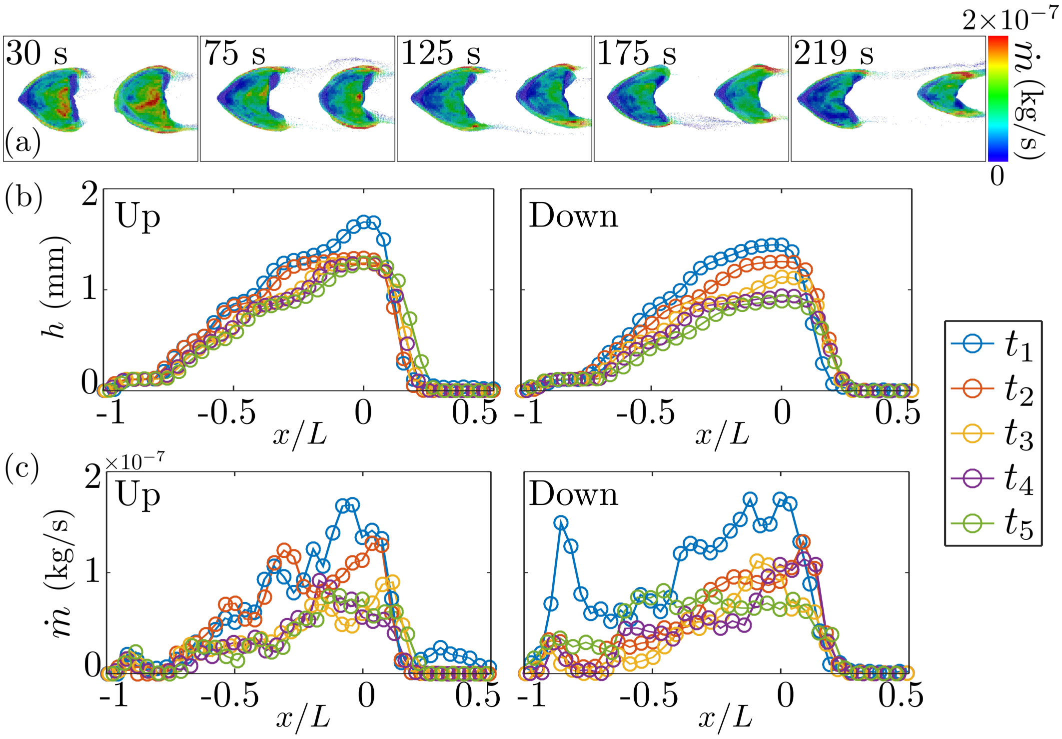

Figure 6. Mass exchange in the aligned case. (a) Snapshots showing the grains of each dune (top view) at different instants, colored in accordance with the average mass flow rate $\dot{m}$ of the region they are in. The averages are computed in intervals t_1 to t_5 (t_1 = 10–50 s, t_2 = 51–100 s, t_3 = 101–150 s, t_4 = 151–200 s, t_5 = 201–238 s). (b) Profiles (height h as a function of the dimensionless longitudinal position x/L with origin at the dune crest) of the centerline for the upstream (Up) and downstream (Down) barchans. (c) Mass flow rate $\dot{m}$ along the barchan by considering its central slice only ($\approx$ 1.2 mm thick), averaged over the t_1 to t_5 intervals, for the upstream (Up) and downstream (Down) barchans.

In addition to velocities and trajectories, we computed averages of the mass flow rate $\dot{m}$ by counting the number of grains moving over the barchans, which we multiplied by their weight and divided by the corresponding time interval and gravity. The averages are computed in the following time intervals: t_1 = 10–50 s, t_2 = 51–100 s, t_3 = 101–150 s, t_4 = 151–200 s, and t_5 = 201–238 s. With that, we end with the space distribution of $\dot{m}$ over both barchans, at different stages of the barchan-barchan interaction. For example, Figures 6a and 7a show top views of the grains of each dune for different time

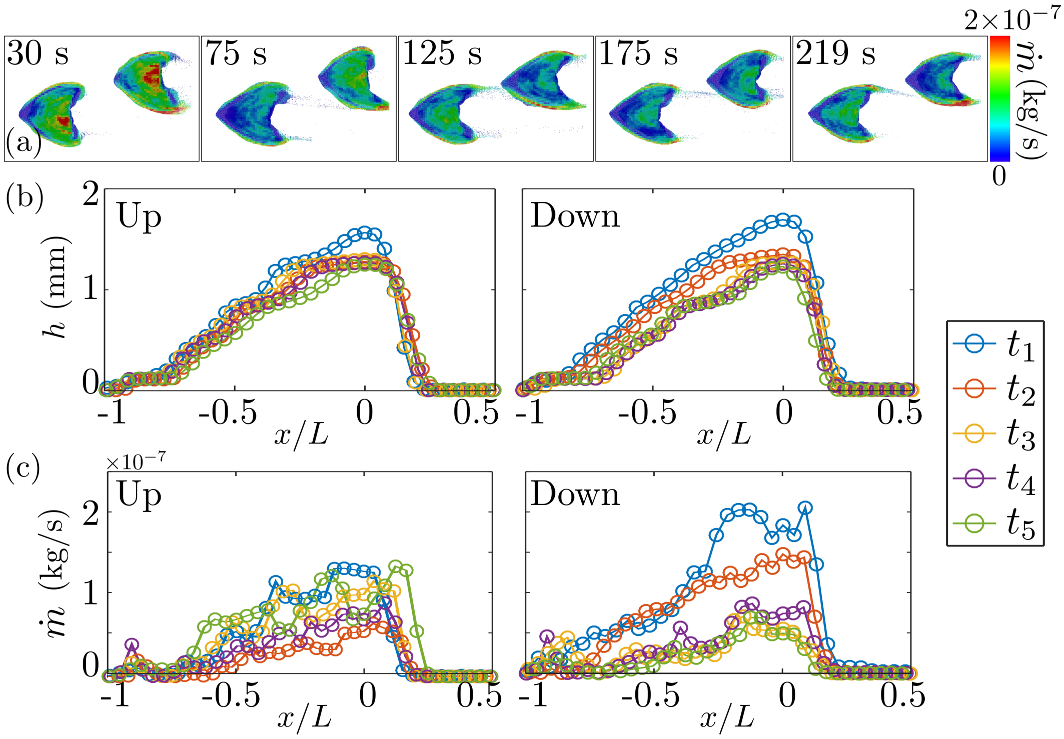

Figure 7. Mass exchange in the off-centered case. (a) Snapshots showing the grains of each dune (top view) at different instants, colored in accordance with the average mass flow rate $\dot{m}$ of the region they are in. The averages are computed in intervals t_1 to t_5 (t_1 = 10–50 s, t_2 = 51–100 s, t_3 = 101–150 s, t_4 = 151–200 s, t_5 = 201–238 s). (b) Profiles (height h as a function of the dimensionless longitudinal position x/L with origin at the dune crest) of the centerline for the upstream (Up) and downstream (Down) barchans. (c) Mass flow rate $\dot{m}$ along the barchan by considering its central slice only ($\approx$ 1.2 mm thick), averaged over the t_1 to t_5 intervals, for the upstream (Up) and downstream (Down) barchans.

instants, colored in accordance with the $\dot{m}$ value of the region they are in, for the aligned and off-centered cases, respectively. We observe that, initially (t_1), $\dot{m}$ is higher over the downstream than on the upstream barchan, indicating higher erosion on the former, with a consequent shrinkage and acceleration with respect to the upstream dune. With this data, it is possible to evaluate how $\dot{m}$ varies longitudinally using, for instance, vertical slices cutting the dune. One slice of interest is that passing by the barchan centerline, for which the dune profiles at different intervals are shown in Figures 6b and 7b for the aligned and off-centered cases, respectively (*Up* referring to the upstream barchan and *Down* to the downstream one). The values of $\dot{m}$ along the longitudinal direction are shown in Figures 6c and 7c, for which we computed $\dot{m}$ by considering a vertical slice $\approx$ 1.2 mm thick. With the exception of the t_1 interval, we observe approximately the same values of $\dot{m}$ for both barchans, while for t_1 the values for the downstream barchan are higher. Values in the certerline are directly related with the dune celerity, since grains in this region spend long times within the barchan, of the order of many turnover times (Zhang et al., 2014). Therefore, because the downstream dune is the smaller one, similar values of $\dot{m}$ in the centerline indicate that it moves faster than the upstream dune, explaining, thus, why the chasing pattern takes place (Assis & Franklin, 2020).

For the aligned case, we note a high peak close to the toe of the downstream barchan ($x/L \approx$ -0.75) during the t_1 interval, which corresponds to the entrainment of grains from the downstream barchan toward the lee side of the upstream dune (as shown in Figure S3 in Supporting Information).

3.3 Resultant force on each grain

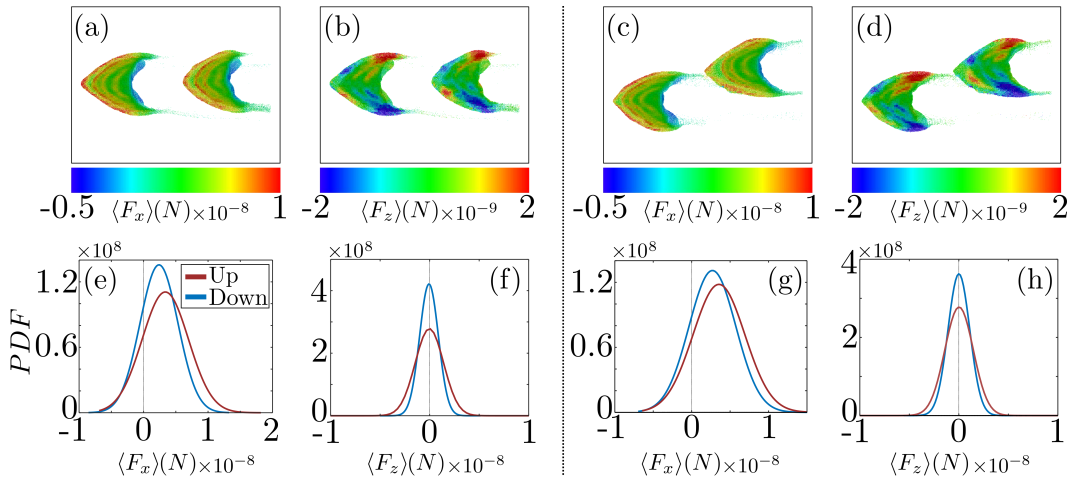

Figure 8. (a)-(d) Top view of dunes colored in accordance with the average resultant force in each region, (a) longitudinal force $\langle F_x \rangle$ for aligned dunes; (b) transverse force $\langle F_z \rangle$ for aligned dunes; (c) $\langle F_x \rangle$ for the off-centered dunes; and (d) $\langle F_z \rangle$ for the off-centered dunes. The averages were computed in the 101-150 s interval, by considering all the grains in each region (including those inside the barchans), and the relative position of morphologies plotted in panels (a)-(d) correspond to t = 125 s. The values of forces in N are presented in the colormap below each panel. (e)-(h) Histograms for the of longitudinal $\langle F_x \rangle$ and transverse $\langle F_z \rangle$ components of forces plotted in the maps of panels (a)-(d), respectively. In the legend, Up and Down stand for upstream and downstream barchans, respectively.

Because we compute Newton's second law for all particles at each time step, the value of the resultant force acting on each grain is available at all instants. This is a great advantage of discrete computations, since this information is inaccessible from experiments and field measurements. Given the large number of particles in our system (initially 10^5 for each dune), we show next plots of the distributions of the resultant force acting on grains, averaged over small time intervals (49 s).

Figures 8a–d show the distributions of time-averaged resultant forces in different regions of the dune, where Figure 8a shows the longitudinal force $\langle F_x \rangle$ for aligned dunes, Figure 8b shows the transverse force $\langle F_z \rangle$ for aligned dunes, Figure 8c shows $\langle F_x \rangle$ for the off-centered dunes, and Fig. 8d shows $\langle F_z \rangle$ for the off-centered dunes. The averages were computed in the 101-150 s interval, by considering all grains in each region (including those inside the barchans), and the values of forces in N can be read on the colormap below each panel. Figures 8e–h show histograms for the of longitudinal $\langle F_x \rangle$ and transverse $\langle F_z \rangle$ components of forces shown in the maps of Figures 8a–d, respectively. Figures of the instantaneous force acting on specific grains along time (Lagrangian tracking), measured as they move from the upstream barchan toward the downstream one, are shown in Figure S6 in Supporting Information. We observe from Figures 8e and 8g that longitudinal forces on grains of both dunes have distributions that are approximately the same, with the most probable value of downstream dunes having a slightly higher peak at slightly lower values. This shows that, throughout the interaction, grains of both dunes experience similar forces and, therefore, accelerations. This is in agreement with the similar values of $\dot{m}$ found over both dunes (Figures 6 and 7). Concerning the transverse component of forces, Figures 8f and 8h show that the most probable values are almost the same for both barchans, with grains on the upstream barchan experiencing a slightly larger range of values.

Interestingly, we observe in Figures 8a and 8c some patterns in the form of curved stripes. Those stripes have approximately the same curvature and wavelength as those formed by bidisperse grains over barchans, reported by Alvarez et al. (2021) and Assis et al. (2022). In these works, the authors attributed the stripes to an instability due to grain segregation only, but the distributions of forces might have an important role in their formation as well, although we do not have a physical explanation for the moment.

3.4 Fluid flow

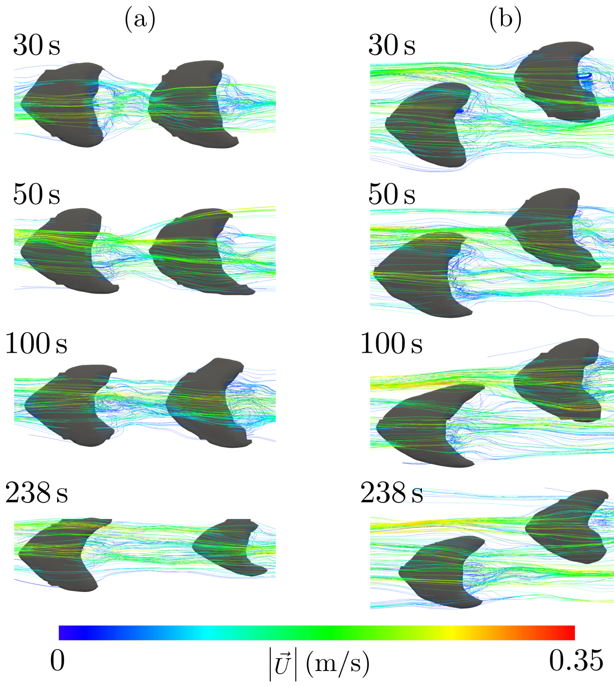

Figure 9. Trajectory lines of the flow over the barchans at different stages of the barchan-barchan interaction for the (a) aligned and (b) off-centered cases. The colors correspond to the magnitude of the velocity of water particles $|\vec{U}|$, the values of which can be read in the colorbar on the bottom of the figure. The corresponding time instants (within the time interval for the considered trajectories) are shown on the top left of each panel.

Finally, we inquire into the fluid flow, which is the mechanism of grain entrainment, and which we computed with a spatial resolution of the order of the grain diameter in the region close to the dune surface. Because of the large quantity of data, we present next typical trajectory lines at different stages of the barchan-barchan interaction.

Figures 9a and 9b show trajectory lines of the water flow over the barchans at different stages of the barchan-barchan interaction, for the aligned and off-centered cases, respectively. These lines shed some light on the behavior of barchans and transport of grains described in previous subsections. For example, for the aligned case, we observe at $t = 30$ s that the recirculation region of the upstream barchan reaches the downstream dune, explaining why grains from the downstream dune migrate toward the upstream one (as shown in Figure S3 in Supporting information). At later times, we observe that the downstream dune shrinks and moves faster than the upstream dune. In addition, initially small asymmetries in the system make the downstream dune to move in the transverse direction ($t = 238$ s, for instance). For the off-centered case, we observe that lines from the free-stream flow impact directly half of the downstream dune (in the case shown, from its toe to the exposed horn on the top of the figure). As a consequence, only the trajectory lines that pass over one side of the upstream dune impact the downstream one, which tends to increase or sustain the asymmetry. In addition, in the region between the horn of the upstream barchan and the toe of the downstream one, the upstream flow arrives disturbed by that horn, with a certain amount of acceleration before impacting the downstream barchan (channeling effect, as shown by Bristow et al., 2018, 2019, 2020), contributing for maintaining the granular mobility and celerity of the downstream barchan. More details on the fluid flow can be seen in Figures S7 to S10 in Supporting Information, where profiles of the mean velocities and second-order moments over both the upstream and downstream barchans are shown.

4 Conclusions

We carried out grain-scale numerical simulations to investigate the mechanisms behind the barchan-barchan repulsion, an interaction pattern known as *chasing* (Assis & Franklin, 2020). We showed that, with the exception of the beginning of interactions, where the mass flow rate $\dot{m}$ is greater over the downstream dune, $\dot{m}$ is roughly the same for both barchans, meaning a higher erosion rate on the downstream dune (since it is smaller due to the higher initial $\dot{m}$). We showed also that in the aligned case a great part of the grains leaving the upstream barchan reach the downstream one, but part of grains of the latter migrate to the upstream dune entrained by its recirculation region. In the off-centered case, only grains from one of the horns of the upstream dune reach the downstream one. The transport of grains is corroborated by the trajectory lines of the fluid, which, in the aligned case, show that the recirculation region of the upstream dune reaches the toe of the downstream barchan and, afterward, small asymmetries make more lines from one side of the upstream dune to reach the downstream one, causing the transverse motion of the latter. In the off-centered case, only approximately half of the lines passing over the upstream barchan reach the downstream dune, increasing or sustaining the off-centered configuration. Interestingly, the velocities of particles is slightly higher over the upstream dune, indicating that the higher erosion over the downstream barchan is due to a higher density of moving particles. Finally, we measured the resultant force acting on each grain and showed that the longitudinal component of time-averaged forces are similar for both dunes. Our results shed light on the reasons for the repulsion characteristic of the chasing pattern, helping to explain why sometimes barchans never touch each other. In addition, our findings can be used to refine current large-scale models (such as continuum models), determine the best sites for placing sensors in field studies or carrying out remote sensing, and feed convolutional neural networks (CNNs) for analyzing large datasets.

Open Research

Data supporting this work were generated by ourselves and are available in Mendeley Data (N. C. Lima et al., 2024) under the CC-BY-4.0 license. The numerical scripts used to post-process the numerical outputs are also available in Mendeley Data (N. C. Lima et al., 2024) under the CC-BY-4.0 license.

Acknowledgments

The authors are grateful to FAPESP (Grant Nos. 2018/14981-7, 2019/10239-7 and 2019/20888-2) and to CNPq (Grant No. 405512/2022-8) for the financial support provided.

References

Alvarez, C. A., Cúñez, F. D., & Franklin, E. M. (2021). Growth of barchan dunes of bidispersed granular mixtures. *Phys. Fluids*, *33*(5), 051705.

Alvarez, C. A., & Franklin, E. M. (2020, Jan). Shape evolution of numerically obtained subaqueous barchan dunes. *Phys. Rev. E*, *101*, 012905. Retrieved from `https://link.aps.org/doi/10.1103/PhysRevE.101.012905` doi: 10.1103/PhysRevE.101.012905

Alvarez, C. A., & Franklin, E. M. (2021). Force distribution within a barchan dune. *Phys. Fluids*, *33*(1), 013313.

Assis, W. R., Cúñez, F. D., & Franklin, E. M. (2022). Revealing the intricate dune-dune interactions of bidisperse barchans. *J. Geophys. Res.: Earth Surf.*, *127*(5), e2021JF006588. Retrieved from `https://agupubs.onlinelibrary.wiley.com/doi/abs/10.1029/2021JF006588` doi: https://doi.org/10.1029/2021JF006588

Assis, W. R., & Franklin, E. M. (2020). A comprehensive picture for binary interactions of subaqueous barchans. *Geophys. Res. Lett.*, *47*(18), e2020GL089464.

Assis, W. R., & Franklin, E. M. (2021). Morphodynamics of barchan-barchan interactions investigated at the grain scale. *J. Geophys. Res.: Earth Surf.*, *126*(8), e2021JF006237.

Bacik, K. A., Lovett, S., Caulfield, C.-c. P., & Vriend, N. M. (2020, Feb). Wake induced long range repulsion of aqueous dunes. *Phys. Rev. Lett.*, *124*, 054501. Retrieved from `https://link.aps.org/doi/10.1103/PhysRevLett.124.054501` doi: 10.1103/PhysRevLett.124.054501

Bagnold, R. A. (1941). *The physics of blown sand and desert dunes.* London: Chapman and Hall.

Berger, R., Kloss, C., Kohlmeyer, A., & Pirker, S. (2015). Hybrid parallelization of the LIGGGHTS open-source DEM code. *Powder Technology*, *278*, 234-247.

Bristow, N. R., Blois, G., Best, J. L., & Christensen, K. T. (2018). Turbulent flow structure associated with collision between laterally offset, fixed-bed barchan dunes. *J. Geophys. Res.-Earth*, *123*(9), 2157-2188.

Bristow, N. R., Blois, G., Best, J. L., & Christensen, K. T. (2019). Spatial scales of turbulent flow structures associated with interacting barchan dunes. *J. Geophys. Res.-Earth*, *124*(5), 1175-1200.

Bristow, N. R., Blois, G., Best, J. L., & Christensen, K. T. (2020). Secondary flows and vortex structure associated with isolated and interacting barchan dunes. *J. Geophys. Res.-Earth*, *125*(2), e2019JF005257.

Claudin, P., & Andreotti, B. (2006). A scaling law for aeolian dunes on Mars, Venus, Earth, and for subaqueous ripples. *Earth Plan. Sci. Lett.*, *252*, 20-44.

Courrech du Pont, S. (2015). Dune morphodynamics. *C. R. Phys.*, *16*(1), 118 - 138.

Durán, O., Schwämmle, V., & Herrmann, H. (2005, Aug). Breeding and solitary wave behavior of dunes. *Phys. Rev. E*, *72*, 021308. Retrieved from `https://link.aps.org/doi/10.1103/PhysRevE.72.021308` doi: 10.1103/PhysRevE.72.021308

Durán, O., Schwämmle, V., Lind, P. G., & Herrmann, H. (2009). The dune size distribution and scaling relations of barchan dune fields. *Granular Matter*, *11*, 7-11.

Elbelrhiti, H., Andreotti, B., & Claudin, P. (2008). Barchan dune corridors: Field characterization and investigation of control parameters. *J. Geophys. Res.:*

Earth Surf., *113*(F2).
Elbelrhiti, H., Claudin, P., & Andreotti, B. (2005). Field evidence for surface-wave-induced instability of sand dunes. *Nature*, *437*(04058).
Endo, N., Taniguchi, K., & Katsuki, A. (2004). Observation of the whole process of interaction between barchans by flume experiments. *Geophys. Res. Lett.*, *31*(12).
Gay, S. P. (1999). Observations regarding the movement of barchan sand dunes in the nazca to tanaca area of southern peru. *Geomorphology*, *27*(3), 279 - 293.
Génois, M., du Pont, S. C., Hersen, P., & Grégoire, G. (2013). An agent-based model of dune interactions produces the emergence of patterns in deserts. *Geophys. Res. Lett.*, *40*(15), 3909-3914.
Génois, M., Hersen, P., du Pont, S., & Grégoire, G. (2013). Spatial structuring and size selection as collective behaviours in an agent-based model for barchan fields. *Eur. Phys. J. B*, *86*(447).
Goniva, C., Kloss, C., Deen, N. G., Kuipers, J. A. M., & Pirker, S. (2012). Influence of rolling friction on single spout fluidized bed simulation. *Particuology*, *10*(5), 582-591.
Herrmann, H. J., & Sauermann, G. (2000). The shape of dunes. *Physica A (Amsterdam)*, *283*, 24-30.
Hersen, P. (2004). On the crescentic shape of barchan dunes. *Eur. Phys. J. B*, *37*(4), 507–514.
Hersen, P., Andersen, K. H., Elbelrhiti, H., Andreotti, B., Claudin, P., & Douady, S. (2004, Jan). Corridors of barchan dunes: Stability and size selection. *Phys. Rev. E*, *69*, 011304. Retrieved from https://link.aps.org/doi/10.1103/PhysRevE.69.011304 doi: 10.1103/PhysRevE.69.011304
Hersen, P., & Douady, S. (2005). Collision of barchan dunes as a mechanism of size regulation. *Geophys. Res. Lett.*, *32*(21).
Hugenholtz, C. H., & Barchyn, T. E. (2012). Real barchan dune collisions and ejections. *Geophys. Res. Lett.*, *39*(2).
Katsuki, A., Kikuchi, M., Nishimori, H., Endo, N., & Taniguchi, K. (2011). Cellular model for sand dunes with saltation, avalanche and strong erosion: collisional simulation of barchans. *Earth Surf. Process. Landforms*, *36*(3), 372-382.
Kloss, C., & Goniva, C. (2010). LIGGGHTS: a new open source discrete element simulation software. In *Proc. 5th int. conf. on discrete element methods.* London, UK.
Kocurek, G., Ewing, R. C., & Mohrig, D. (2010). How do bedform patterns arise? new views on the role of bedform interactions within a set of boundary conditions. *Earth Surf. Process. Landforms*, *35*(1), 51-63.
Lima, A., Sauermann, G., Herrmann, H., & Kroy, K. (2002). Modelling a dune field. *Physica A*, *310*(3), 487-500. Retrieved from https://www.sciencedirect.com/science/article/pii/S0378437102005460
Lima, N. C., Assis, W. R., Alvarez, C. A., & Franklin, E. M. (2022). Grain-scale computations of barchan dunes. *Phys. Fluids*, *34*(12), 123320. Retrieved from https://doi.org/10.1063/5.0121810 doi: 10.1063/5.0121810
Lima, N. C., Assis, W. R., & Franklin, E. M. (2024). Numerical simulation of barchan-barchan repulsion [Dataset][Software]. *Mendeley Data, http://dx.doi.org/10.17632/ypkgwjfr4r.1*. doi: 10.17632/ypkgwjfr4r.1
Liu, D., Liu, X., Fu, X., & G., W. (2016). Quantification of the bed load effects on turbulent open-channel flows. *J. Geophys. Res. Earth Surf.*, *121*, 767-789.
Norris, R. M., & Norris, K. S. (1961). Algodones Dunes of Southeastern California. *GSA Bulletin*, *72*(4), 605-619.
Parteli, E., & Herrmann, H. (2003). A simple model for a transverse dune field. *Physica A*, *327*(3), 554-562.
Parteli, E. J. R., & Herrmann, H. J. (2007, Oct). Dune formation on the present mars. *Phys. Rev. E*, *76*, 041307. Retrieved from https://link.aps.org/doi/

10.1103/PhysRevE.76.041307 doi: 10.1103/PhysRevE.76.041307

Schwämmle, V., & Herrmann, H. J. (2003). Solitary wave behaviour of sand dunes. *Nature*, *426*, 619-620.

Tsuji, Y., Kawaguchi, T., & Tanaka, T. (1993). Discrete particle simulation of two-dimensional fluidized bed. *Powder Technology*, *77*(1), 79-87.

Tsuji, Y., Tanaka, T., & Ishida, T. (1992). Lagrangian numerical simulation of plug flow of cohesionless particles in a horizontal pipe. *Powder Technology*, *71*(3), 239-250.

Vermeesch, P. (2011). Solitary wave behavior in sand dunes observed from space. *Geophys. Res. Lett.*, *38*(22).

Zhang, D., Yang, X., Rozier, O., & Narteau, C. (2014). Mean sediment residence time in barchan dunes. *J. Geophys. Res.: Earth Surf.*, *119*(3), 451–463.

Zhou, X., Wang, Y., & Yang, B. (2019). Three-dimensional numerical simulations of barchan dune interactions in unidirectional flow. *Particul. Sci. Technol.*, *37*(7), 835-842.

Zhou, Z. Y., Kuang, S. B., Chu, K. W., & Yu, A. B. (2010). Discrete particle simulation of particle–fluid flow: model formulations and their applicability. *J. Fluid Mech.*, *661*, 482–510.